

## Microscale 3D Printed Pillars and Porous Polymeric Structures Manufacturability and Micromechanics

Isaakidou, Aikaterini; Ganjian, Mahya; Moosabeiki, Vahid; Leeflang, Marius Alexander; Goushki, Mahdiyeh Nouri; Boukany, Pouyan Esmailzadeh; Wątroba, Maria; Groetsch, Alexander; Schwiedrzik, Jakob; Mirzaali, Mohammad Javad

### DOI

[10.1002/adem.202500977](https://doi.org/10.1002/adem.202500977)

### Publication date

2025

### Document Version

Final published version

### Published in

Advanced Engineering Materials

### Citation (APA)

Isaakidou, A., Ganjian, M., Moosabeiki, V., Leeflang, M. A., Goushki, M. N., Boukany, P. E., Wątroba, M., Groetsch, A., Schwiedrzik, J., Mirzaali, M. J., Apachitei, I., Fratila-Apachitei, L. E., & Zadpoor, A. A. (2025). Microscale 3D Printed Pillars and Porous Polymeric Structures: Manufacturability and Micromechanics. *Advanced Engineering Materials*, Article e202500977. <https://doi.org/10.1002/adem.202500977>

### Important note

To cite this publication, please use the final published version (if applicable).  
Please check the document version above.

### Copyright

Other than for strictly personal use, it is not permitted to download, forward or distribute the text or part of it, without the consent of the author(s) and/or copyright holder(s), unless the work is under an open content license such as Creative Commons.

### Takedown policy

Please contact us and provide details if you believe this document breaches copyrights.  
We will remove access to the work immediately and investigate your claim.

# Microscale 3D Printed Pillars and Porous Polymeric Structures: Manufacturability and Micromechanics

Aikaterini Isaakidou,\* Mahya Ganjian, Vahid Moosabeiki, Marius Alexander Leeftang, Mahdijeh Nouri Goushki, Pouyan Esmailzadeh Boukany, Maria Wątroba, Alexander Groetsch, Jakob Schwiedrzik, Mohammad Javad Mirzaali, Iulian Apachitei, Lidy Elena Fratila-Apachitei,\* and Amir Abbas Zadpoor

Two-photon polymerization (2PP) is an additive manufacturing technology capable of producing polymeric 3D nano- to mesoscale structures with design flexibility and sub-micron resolution. This study investigates the influence of 2PP printing parameters on the morphology and mechanical properties of solid and porous microstructures fabricated from three commercial resins: IP-Q, IP-S, and IP-polydimethylsiloxane (IP-PDMS). To evaluate micromechanical behavior, micropillar compression tests are conducted using IP-Q, which has not been extensively characterized. Porous structures retained 80–85% of the stiffness of solids for IP-Q and IP-S, and 50% for IP-PDMS. Fourier transform infrared spectroscopy showed degrees of conversion of 38% for IP-Q and 61% for IP-S and IP-PDMS. The optimal printing parameters for IP-Q micropillars were a laser power of 50 mW, slicing distance ( $s$ ) of 1.2  $\mu\text{m}$ , and hatching distance ( $h$ ) of 1  $\mu\text{m}$ . These settings correspond to a peak laser intensity of  $1.58 \times 10^{-11} \text{ W cm}^{-2}$ , a focal spot diameter ( $d_{xy}$ ) of 3.17  $\mu\text{m}$ , a Rayleigh length ( $z_R$ ) of 10.13  $\mu\text{m}$ , and a voxel overlap ( $\delta$ ) of 0.6. These conditions yielded a Young's modulus of 3.7 GPa and yield strength of 75.21 MPa. Overall, the findings emphasize the challenges of parameter optimization when introducing porosity and comparing materials. The results provide a systematic framework for tailoring 2PP processing to guide biomedical microdevice design.

3D micro- and nanoscale structures.<sup>[1]</sup> The working principle of 2PP is based on the nonlinear absorption of two photons, allowing for the deposition of near-infrared femtosecond laser energy into a volume of a photosensitive material.<sup>[2]</sup> The quadratic relationship of two-photon absorption with light intensity provides high precision and resolution by enabling precise control of the crosslinking photoreaction, ensuring that polymerization only occurs within the localized focal region (i.e., voxel).<sup>[3]</sup> This fine control over the fabrication process is particularly advantageous for creating 3D microstructures with a high level of detail, which is essential for tissue engineering applications and drug delivery systems.<sup>[2]</sup> A wide range of materials can be used in the two-photon fabrication, including polyacrylic resins, hydrogels, epoxides, and inorganic/organic polymers.<sup>[4,5]</sup>


The selection of suitable materials for biomedical applications (Figure 1C) is broadened by the increased availability of diverse 2PP materials and their characteristics. The biocompatibility of such materials

is a critical factor, necessitating investigations into the interactions between the materials, living tissues<sup>[6]</sup> and cells.<sup>[7]</sup> Additionally, the mechanical properties and printing resolution are crucial factors in determining their suitability for specific

## 1. Introduction

Two-photon polymerization (2PP) has emerged as a cutting-edge technology with the compelling advantage of producing complex

A. Isaakidou, M. Ganjian, V. Moosabeiki, M. A. Leeftang, M. J. Mirzaali, I. Apachitei, L. E. Fratila-Apachitei, A. A. Zadpoor  
 Department of Biomechanical Engineering  
 Faculty of Mechanical Engineering  
 Delft University of Technology (TU Delft)  
 Mekelweg 2, Delft 2628 CD, The Netherlands  
 E-mail: A.Isaakidou@tudelft.nl; E.L.Fratila-Apachitei@tudelft.nl

 The ORCID identification number(s) for the author(s) of this article can be found under <https://doi.org/10.1002/adem.202500977>.

© 2025 The Author(s). Advanced Engineering Materials published by Wiley-VCH GmbH. This is an open access article under the terms of the Creative Commons Attribution License, which permits use, distribution and reproduction in any medium, provided the original work is properly cited.

DOI: 10.1002/adem.202500977

M. Wątroba, A. Groetsch, J. Schwiedrzik  
 Empa  
 Swiss Federal Laboratories for Materials Science and Technology  
 Laboratory of Mechanics of Materials and Nanostructures  
 Feuerwerkerstrasse 39, Thun CH-3602, Switzerland

M. N. Goushki, P. E. Boukany  
 Department of Chemical Engineering  
 Faculty of Applied Sciences  
 Delft University of Technology (TU Delft)  
 Van der Maasweg 9, Delft 2629 HZ, The Netherlands

A. Groetsch  
 Department of Materials Science and Engineering  
 Henry Samueli School of Engineering  
 University of California  
 Irvine CA 92697, USA

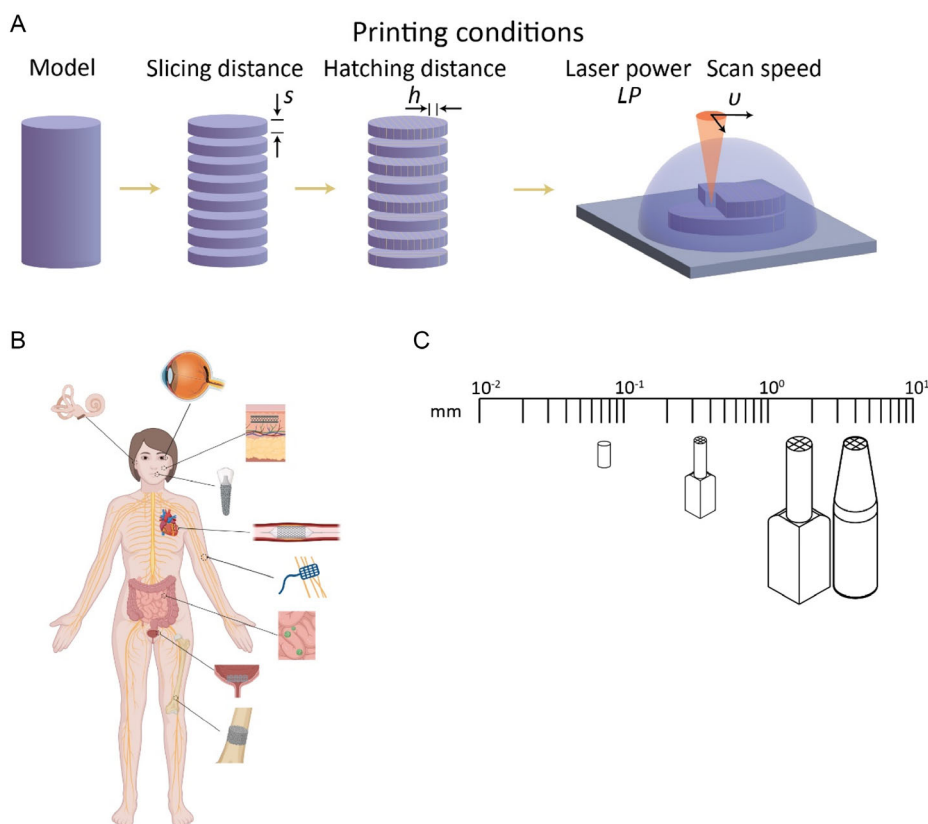


**Figure 1.** A) A schematic representation of the printing conditions (i.e., slicing and hatching distance, laser power, and scanning speed) that govern the 2PP printing process. B) Human body anatomy with details on organs that can benefit from porous medical devices in various scales and materials. C) The versatility of the 2PP method allows for printing across different scales and materials for biomedical applications.

applications.<sup>[8]</sup> Studies on the Young's modulus,  $E$ , of various commercially available photoresists often consider the printing conditions (Figure 1A), such as hatching and slicing distance, laser power (LP), and scanning speed, as these influence crosslinking.<sup>[8–11]</sup> The Young's moduli of polyacrylic resins, epoxides, and inorganic/organic polymers are generally reported to be in the GPa range, while those of hydrogels tend to be in the kPa range.<sup>[12]</sup> Optimizing the printing conditions is essential to ensure mechanical stability and versatility across various materials, shapes, and scales (Figure 1B). For example, recent advances in continuous scanning have even enabled high-resolution fabrication across five orders of magnitude. This approach extends the applicability of 2PP into the mesoregime, allowing for the fabrication of centimeter-scale objects with microscale or even nanoscale decorations.<sup>[13]</sup>

In this study, we focus on the printing and mechanical characterization of solid and porous microstructures inspired by a recently developed cochlear implant design.<sup>[14]</sup> The structures were fabricated using three photocurable resins: acrylate-based IP-Q, IP-S, and the hybrid polydimethylsiloxane- and acrylate-based IP-PDMS resin (Nanoscribe GmbH & Co. KG, Karlsruhe, Germany). These resins were selected to represent a broad range of mechanical properties, with IP-Q and IP-S exhibiting elastic moduli of 3.17<sup>[11]</sup> and 4.6 GPa,<sup>[15]</sup> respectively, and IP-PDMS, a compliant elastomer with a much lower elastic modulus of

17.8 MPa.<sup>[16]</sup> This range of mechanical properties makes the study of the selected resins relevant for diverse biomedical applications, from load-bearing permanent structures to soft, compliant microsystems.

We aim to provide insights into material selection, optimization of 2PP printing settings, and mechanical properties of the printed 3D microstructures. These structures could be relevant for applications in microfluidics,<sup>[17,18]</sup> drug delivery,<sup>[19,20]</sup> and tissue engineering.<sup>[21,22]</sup> For example, in drug delivery applications, porosity is a crucial factor to consider, as it affects drug loading, release kinetics, and bioavailability. Encapsulation of drugs within porous matrices can enhance stability, solubility, and dissolution rates, while allowing precise control over drug release. This approach improves cellular uptake and therapeutic efficacy, and minimizes side effects.<sup>[23,24]</sup> The present study does not focus on the fabrication of ready-to-use biomedical devices, but rather systematically generates knowledge on how 2PP processing parameters influence the manufacturability, geometry, and micromechanical response of selected commercial resins. This exploration provides a foundation for future device-specific evaluations.

Using all three previously mentioned photoresists, we developed printing methods to manufacture microstructures that were either solid or exhibited confined microporosity. We then characterized the morphology, chemistry, and mechanics of the

resulting solid and porous microarchitectures. To our knowledge, no systematic investigation has been conducted on how 2PP printing parameters affect the shape fidelity, chemistry, and mechanical properties of the IP-Q material. Therefore, we performed further mechanical characterization of IP-Q micropillars printed with varying parameters through compression testing. A key aspect of the current study is the use of microcompression to assess the mechanical properties of IP-Q material. In contrast to our previous study,<sup>[25]</sup> where mechanical characterization of IP-Q structures required enlarging the corresponding structures to perform mechanical testing and to combine them with finite element analysis (FEA) models for validation, the current method enabled direct assessment of the material properties of IP-Q. Mechanical properties from such printed solid structures are important input parameters for constitutive models. Thus, our results provide valuable new data for researchers working with the 2PP resins included in this study that can be used for microfluidics, cell scaffold applications, and drug delivery systems.

## 2. Experimental Section

### 2.1. 2PP Printing of Microscale Structures Using IP-Q, IP-S, and IP-PDMS

Computer-aided design (CAD) models of solid and porous microscale structures, based on recently developed cochlear implant models<sup>[14]</sup> with dimensions  $86 \times 86 \times 343 \mu\text{m}^{-3}$  and a tip diameter of  $50 \mu\text{m}$ , were created using SolidWorks (Dassault Systèmes SE, Vélizy-Villacoublay, France) and nTopology 3.35 (nTopology Inc., New York, NY, USA), respectively. Using Nanoscribe's Describe software, the designs were used to create the printing job file for the direct laser writing system (Photonic Professional GT, Nanoscribe GmbH, Eggenstein-Leopoldshafen, Germany) operating with a pulsed femtosecond laser (wavelength =  $780 \text{ nm}$ , pulse duration =  $100 \text{ fs}$ , with a repetition rate of  $80 \text{ MHz}$ , Galvo writing mode). For printing with the IP-Q resin, a droplet of resin was applied to a silicon substrate and then exposed to the laser beam using a  $10\times$  objective ( $\text{NA} = 0.3$ ). For IP-S and IP-PDMS, a droplet of resin was applied to ITO-coated substrates and then exposed to the laser beam using a  $25\times$  objective ( $\text{NA} = 0.8$ ). Different printing conditions were explored to identify optimal parameters for repeatable and stable prints of solid and porous models for each resin type (Table 1). For each resin and condition (solid and porous), three representative microstructures were fabricated and characterized ( $n = 3$ ). All structures were fabricated in a vertical orientation,

**Table 1.** Printing parameters for microstructures made with IP-Q, IP-S, and IP-PDMS. The best settings for printing porous and solid microstructures are given in bold (LP: laser power,  $v$ : scanning speed,  $h$ : hatching distance,  $s$ : slicing distance).

	LP [mW]	$v$ [ $\text{mm s}^{-1}$ ]	$h$ [ $\mu\text{m}$ ]	$s$ [ $\mu\text{m}$ ]
IP-Q	20, 30, 40	150	0.2	0.2
IP-S	20, 30, 40	150	0.2	0.2
IP-PDMS	35, 42.5, 50	100	0.4	0.4

aligned with the laser axis. The slicing distance ( $s$ ) and hatching distance ( $h$ ) were set to  $0.2 \mu\text{m}$  for IP-Q and IP-S and  $0.4 \mu\text{m}$  for IP-PDMS. The scanning speed ( $v$ ) was set at  $150 \text{ mm s}^{-1}$  for IP-Q and IP-S and  $100 \text{ mm s}^{-1}$  for IP-PDMS. LP was varied to investigate its effect, ranging from 20 to  $40 \text{ mW}$  in  $10 \text{ mW}$  increments for IP-Q and IP-S, and from 35 to  $50 \text{ mW}$  in  $7.5 \text{ mW}$  increments for IP-PDMS. For the IP-Q structures, following exposure, the development process involved immersion of the prints for 25 min in propylene glycol monomethyl ether acetate (PGMEA, Sigma-Aldrich, Darmstadt, Germany), a 5 min rinse in isopropyl alcohol (IPA, Sigma-Aldrich, Darmstadt, Germany), and drying with an air gun. For the IP-S structures, the development process involved immersing the prints in PGMEA for 20 min, followed by 30 s in methoxy-nonafluorobutane (Novec 7100, Sigma-Aldrich, Darmstadt, Germany), and then drying with an air gun. In the case of the IP-PDMS structures, the development involved immersing the prints in IPA for 5 min, followed by drying with an air gun.

### 2.2. 2PP Printing of Micropillars Using IP-Q

Micropillars with a diameter of  $D = 50 \mu\text{m}$  and a height of  $H = 100 \mu\text{m}$  were designed using SolidWorks (Dassault Systèmes SE, Vélizy-Villacoublay, France). The scanning speed ( $v$ ) was set to  $100 \text{ mm s}^{-1}$ . Two groups were investigated: In the first group, the slicing distance ( $s$ ) was fixed at  $5 \mu\text{m}$  while the hatching distance ( $h$ ) was varied from  $0.4$  to  $3.4 \mu\text{m}$  in  $0.6 \mu\text{m}$  steps; in the second group, the hatching distance was fixed at  $1 \mu\text{m}$  while the slicing distance was varied from  $1.2$  to  $7.5 \mu\text{m}$  in  $1.26 \mu\text{m}$  increments. The LP was varied between 20 and  $60 \text{ mW}$  in  $10 \text{ mW}$  increments for both groups (Table 2). For each of the above mentioned conditions, one representative micropillar was fabricated and characterized ( $n = 1$ ). Preparation for printing and development of the printed micropillars was performed according to the experimental procedure for IP-Q described in Section 2.1 of Experimental Section.

### 2.3. Morphological Characterization of Microscale Structures and Micropillars

Structural characterization of the printed samples was done by scanning electron microscopy (SEM) (FEI Helios G4 CX dual-beam workstation, Hillsborough, OR, USA). Before SEM imaging, the samples were gold sputtered (gold layer thickness  $\approx 5 \text{ nm}$ ) using a sputter coater (JFC-1300, JEOL, Akishima, Japan). The influence of this gold layer on the mechanical behavior of the samples is negligible.<sup>[26]</sup> Focused ion beam SEM (FIB-SEM) (FEI, Helios Nano Lab 650, Hillsborough, OR, USA)

**Table 2.** Printing parameters for the micropillars made with IP-Q (LP: laser power,  $v$ : scanning speed,  $h$ : hatching distance,  $s$ : slicing distance).

Printing parameter	IP-Q
LP [mW]	20, 30, 40, 50, 60
$v$ [ $\text{mm s}^{-1}$ ]	100
$h$ [ $\mu\text{m}$ ]	0.4, 1.0, 1.6, 2.2, 2.8, 3.4
$s$ [ $\mu\text{m}$ ]	1.2, 2.5, 3.7, 5.0, 6.2, 7.5

was used to examine the pore morphology and calculate the apparent porosity and relative density of the 3D porous microstructures. To image the pores longitudinal cross-sections of the samples were prepared by FIB (current: 0.17 nA, voltage: 30 kV).

## 2.4. Chemical Characterization of IP-Q, IP-S, and IP-PDMS

The elemental composition of IP-Q, IP-S, and IP-PDMS resins was quantified using X-ray photoelectron spectroscopy (XPS) (Thermo Fisher K-Alpha instrument, Rockford, IL, USA). Each sample was scanned four times, with an energy step of 0.4 eV, utilizing an Al K $\alpha$  source gun with a spot size of 400  $\mu\text{m}^{-2}$ . To identify the functional groups in the different photoresists before and after polymerization and to assess the degree of conversion (DC), Fourier transform infrared spectroscopy (FTIR) was used (Nicolet FTIR spectrometer 6700, Thermo Fisher Scientific in Waltham, MA, USA). The spectra acquisition spanned the range of 4000–463  $\text{cm}^{-1}$ . The DC was determined by measuring the change in the absorbance peak height of the bonds most relevant to the polymerization of the resins, according to,<sup>[27]</sup>

$$DC = \left(1 - \frac{A_P}{A_R}\right) \times 100\% \quad (1)$$

where  $A_P$  is the absorbance of the sample after polymerization (printed structure) and  $A_R$  is the absorbance of the unpolymerized resin.

## 2.5. Compression of Microscale Structures and Micropillars

The IP-Q and IP-S microstructures were compressed using an ex situ indenter setup developed at Empa (Thun, Switzerland) and based on commercial hardware for actuation, sensing, and electronics (Alemnis AG, Thun, Switzerland). These experiments were conducted at ambient temperature and humidity, using a flat punch diamond tip (diameter = 150  $\mu\text{m}$ , 60° cone angle) (Synton MDP, Nidau, Switzerland). The microstructures were compressed uniaxially using a quasistatic displacement-controlled loading protocol at a displacement rate of 50  $\text{nm s}^{-1}$  and up to 10% of engineering strain. The stiffness of the microstructures was extracted from the best linear fit of the loading segment of the load-displacement curves.

For the IP-PDMS microstructures, compression was conducted using a Piuma nanoindenter (Optics11 Life B.V., Amsterdam, The Netherlands), which featured a sphere-shaped tip with a radius of 48  $\mu\text{m}$  (able to cover the tip of the structures) and a measured and calibrated stiffness of 3.89  $\text{N m}^{-1}$ . Compression was repeated nine times in a grid pattern to ensure complete coverage of the specimen's tip ( $d = 50 \mu\text{m}$ ), with a 5  $\mu\text{m}$  displacement for each step. This test was conducted for four printed samples. According to the manufacturer's instructions<sup>[28]</sup> the samples were submerged in demineralized water throughout the test to avoid adhesion of the probe and the sample. An indentation-controlled procedure was followed for these measurements, with a maximum indentation depth of 5000 nm, a displacement rate of 500  $\text{nm s}^{-1}$ , and a retraction speed of 5000  $\text{nm s}^{-1}$ . The force-displacement curves were analyzed, and the data was extracted from the best linear fit of the loading part of the curves.

The IP-Q micropillars were tested by applying the same tip specifications and ambient conditions as the IP-Q and IP-S microstructures. They were compressed uniaxially using a quasistatic displacement-controlled loading protocol at a displacement rate of 50  $\text{nm s}^{-1}$  and up to 36.5% of engineering strain. The engineering strain ( $\epsilon$ ) was calculated based on the recorded displacement data and the initial height of each micropillar, determined by high-resolution SEM imaging. The engineering stress was then calculated by dividing the recorded load data by the top surface area of the structures. The yield stress ( $\sigma_y$ ) was determined using the 0.2% offset criterion. The elastic modulus ( $E$ ) was extracted from the loading segment of the stress-strain curves before the yield point using linear regression.

## 2.6. Statistical Analysis

To investigate whether there is a significant difference in the stiffness between the solid and porous counterparts of the microstructures fabricated by IP-Q, IP-S, and IP-PDMS, we conducted unpaired  $t$ -tests ( $p \leq 0.05$ ). We assessed the normality of the data using the Shapiro-Wilk test ( $p \leq 0.05$ ), which is appropriate for the small sample size in our study. The results of these normality tests for the stiffness values are presented in (Figure S1, Supporting Information). We applied one-way ANOVA analysis (Table S2, Supporting Information) and the Tukey's multiple comparisons test (Table S3, Supporting Information) to assess the cross-material comparison amongst our groups. The data was analyzed using Prism 10 (GraphPad Software Inc., San Diego, CA, United States).

# 3. Results

## 3.1. Morphological Characterization of Microscale Structures

A parametric study was performed to determine suitable printing parameters for a repeatable fabrication of the microscale structures from each resin (Figure 2). Porous structures from IP-PDMS printed with  $h = s = 0.4 \mu\text{m}$ ,  $v = 150 \text{ mm s}^{-1}$ , and LP = 35 or 50 mW exhibited defects on both their tip and main body. Random resin protrusions were observed on their tip, and dents on their main trunk revealed their inner porous structure (Figure 2C). IP-PDMS structures printed with LP = 42.5 mW exhibited improved overall quality with fewer manufacturing imperfections (Figure 2C). Examination through FIB milling of the porous structures revealed well-formed internal pores (Figure 2D). The parametric study on the microstructures made by IP-Q and IP-S did not reveal outer morphological differences in different printing settings. Although the exact sizes of the pores could not be accurately quantified from the FIB/SEM images, the parametric study indicated the window of printing conditions (see also Table 1) that can be used for each type of resin to generate stable and reproducible solid and porous microscale structures.

## 3.2. Morphological Characterization of Micropillars

Since the process-structure-mechanics relationship for the 2PP printed IP-Q material had not been previously studied, a more



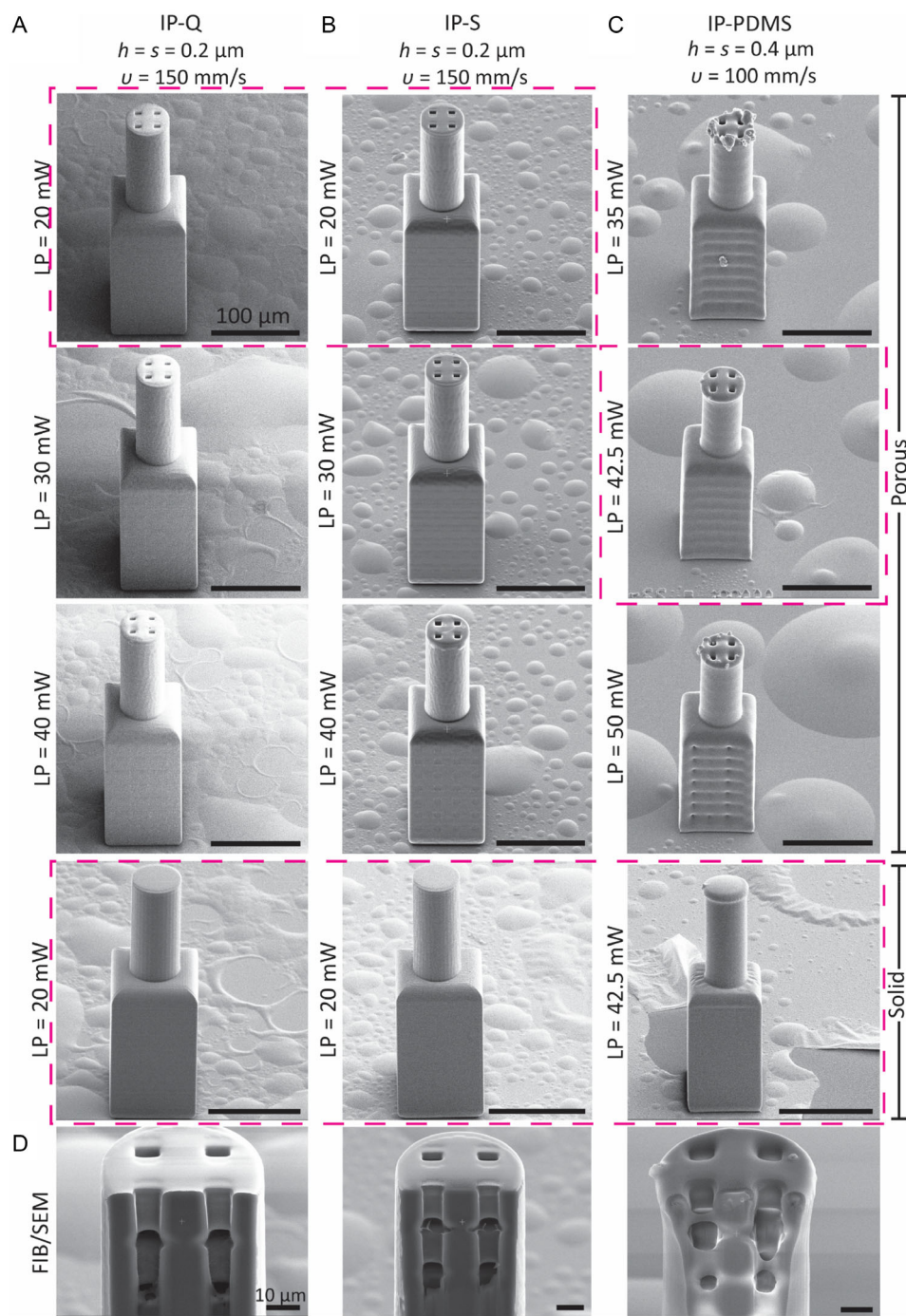


**Figure 2.** Tilt-view (52°) SEM images of 2PP printed porous and solid microstructures with varying laser powers (LP = 20–50 mW) made from A) IP-Q (left), B) IP-S (middle), and C) IP-PDMS (right) resin (scale bar = 100 μm). The dashed lines enclose the highest-quality prints. D) The FIB milling of porous microstructures fabricated using the mentioned resins demonstrates the embedding of pores (scale bar = 10 μm).

detailed parametric study was conducted, and the results were used to understand the mechanical properties of the printed samples. Therefore, a first series of IP-Q micropillars were fabricated by varying the LP and slicing distance while keeping the hatching distance ( $h = 1 \mu\text{m}$ ) and scanning speed ( $v = 100 \text{ mm s}^{-1}$ ) constant (Figure 3). When using a LP of

LP = 20 mW and a slicing distance of  $s = 7.5 \mu\text{m}$ , no micropillars formed on the substrate (Figure 3), indicating that the processing parameters were unsuitable for initiating photopolymerization. As the slicing distance decreased, micropillars began to form. Lower slicing distances resulted in micropillars with dimensions closer to the designed specifications ( $D = 50 \mu\text{m}$ ,  $H = 100 \mu\text{m}$ );

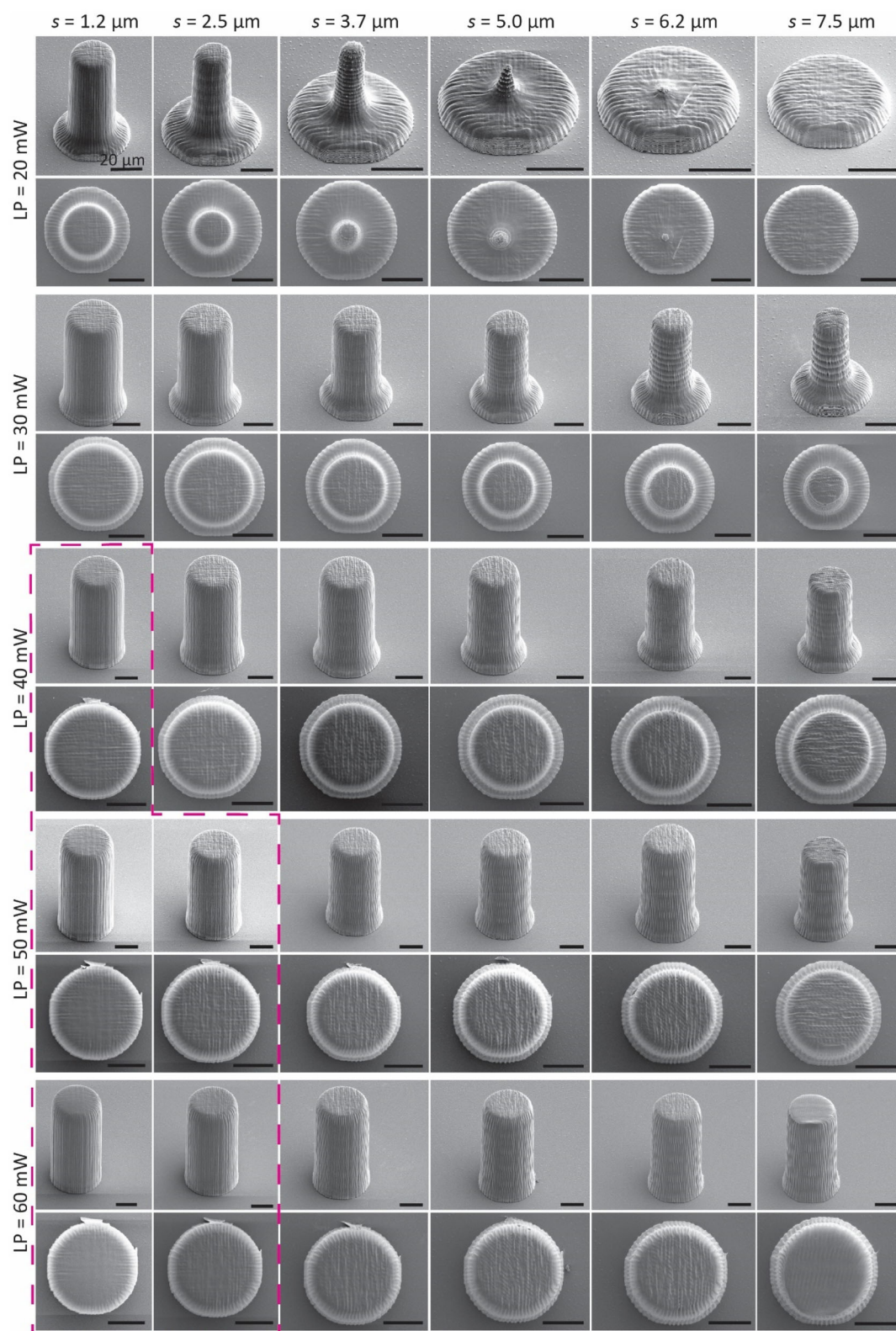


**Figure 3.** Top and tilt-view (52°) SEM images of 2PP-printed IP-Q micropillars fabricated with varying slicing distance ( $s = 1.2\text{--}7.5 \mu\text{m}$ ) and laser power (LP = 40–120%) for constant hatching distance ( $h = 1 \mu\text{m}$ ) and scanning speed ( $v = 100 \text{ mm s}^{-1}$ ) (scale bar = 20  $\mu\text{m}$ ). The dashed lines enclose the highest-quality prints.



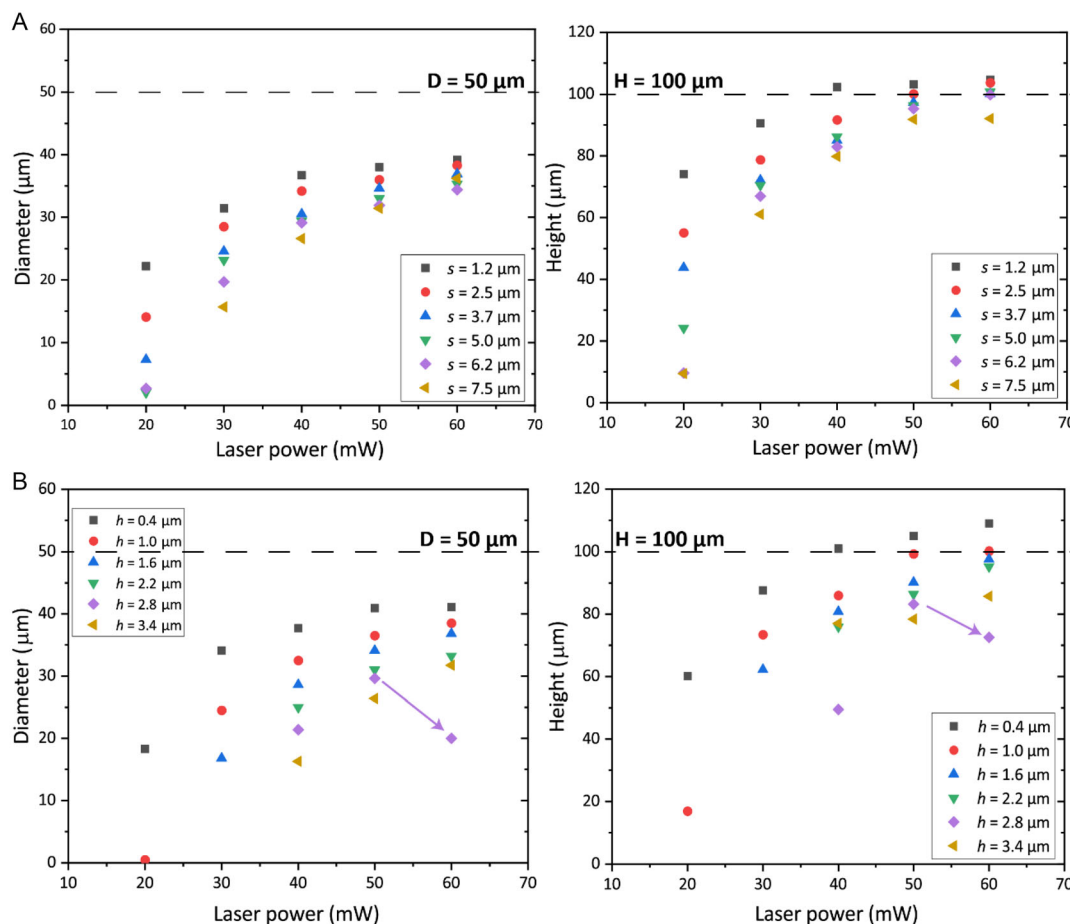


**Figure 4.** A) Effects of laser power (LP) and slicing distance ( $s$ ) on the diameter ( $D$ ) and height ( $H$ ) of micropillars fabricated using IP-Q and B) effects of LP and hatching distance ( $h$ ) on  $D$  and  $H$  of the micropillars fabricated using IP-Q.

however, they did not reach the target dimensions for  $D$  (Figure 4A). Generally, with  $LP > 30$  mW, micropillars can be printed even with larger slicing distances, although their dimensions deviate from the designed values (Figure 4A). For  $LP \geq 40$  mW and for  $s \leq 2.4$   $\mu\text{m}$  the diameter of the pillars deviated by 22%–32% (Table S6, Supporting Information) from the designed one ( $D = 39.2$   $\mu\text{m}$ ). The largest diameter achieved was at  $LP = 60$  mW and for  $s = 1.2$   $\mu\text{m}$ . At the largest diameter settings, the pillar's height was measured to be  $\approx 5\%$  larger than the designed one, thus 104.6  $\mu\text{m}$ . A second batch of IP-Q micropillars was fabricated to investigate the effect of varying LP and hatching distance, while maintaining a constant slicing distance ( $s = 5$   $\mu\text{m}$ ) and scanning speed ( $v = 100$   $\text{mm s}^{-1}$ ) (Figure 5). LP values of  $LP = 20$  mW did not result in the fabrication of stable micropillars. By increasing the LP to 30 mW, micropillars were formed for low hatching distances ( $h = 0.4$  and  $1.0$   $\mu\text{m}$ ). Increasing the hatching distance ( $h = 2.2$ – $3.4$   $\mu\text{m}$ ) decreased the chance of polymerization, making the fabricated micropillars unstable enough to stand vertically on the substrate, which led to bending (Figure 5). When  $LP > 40$  mW, micropillars formed for all chosen hatching distances (Figure 5). Similarly to the investigation on the slicing distance, smaller hatching distances resulted in dimensions closer to the designed ones.

For  $LP \geq 40$  mW and  $h \leq 1.6$   $\mu\text{m}$ , the diameter of the pillars deviated by 18%–43% (Table S6, Supporting Information) from the designed one. The largest diameter achieved was at  $LP = 60$  mW and  $h = 0.4$   $\mu\text{m}$  ( $D = 41.1$   $\mu\text{m}$ ), and at those settings, the height of the micropillar was  $H = 109$   $\mu\text{m}$ , 9% larger than designed. Generally, the higher the LP and the smaller the slicing and hatching distance values, the closer the dimensions were to the designed values (Figure 4B). However, for  $s = 5$   $\mu\text{m}$  and  $h = 2.8$   $\mu\text{m}$ , both the pillar diameter and height increased until  $LP = 50$  mW, but for  $LP = 60$  mW, there is a drop in the resulting  $D$  and  $H$  values (purple arrows on Figure 4B).

### 3.3. Chemical Characterization of IP-Q, IP-S, and IP-PDMS

A survey scan was performed to identify elements other than C, O, and N in all the resins (Figure 6A). The IP-S and IP-Q samples are similar, and their XPS survey graphs overlap. The IP-PDMS survey scan clearly shows the presence of Si and confirms the presence of the monomer  $\text{Si}(\text{CH}_3)_2\text{O}$ . The spectrum shows a peak centered around 284.47 eV for IP-S (Figure 6B). For IP-Q, the spectrum is centered around 284.10 eV (Figure 6C), corresponding to the C1s bond. For IP-PDMS, the C1s bond is found



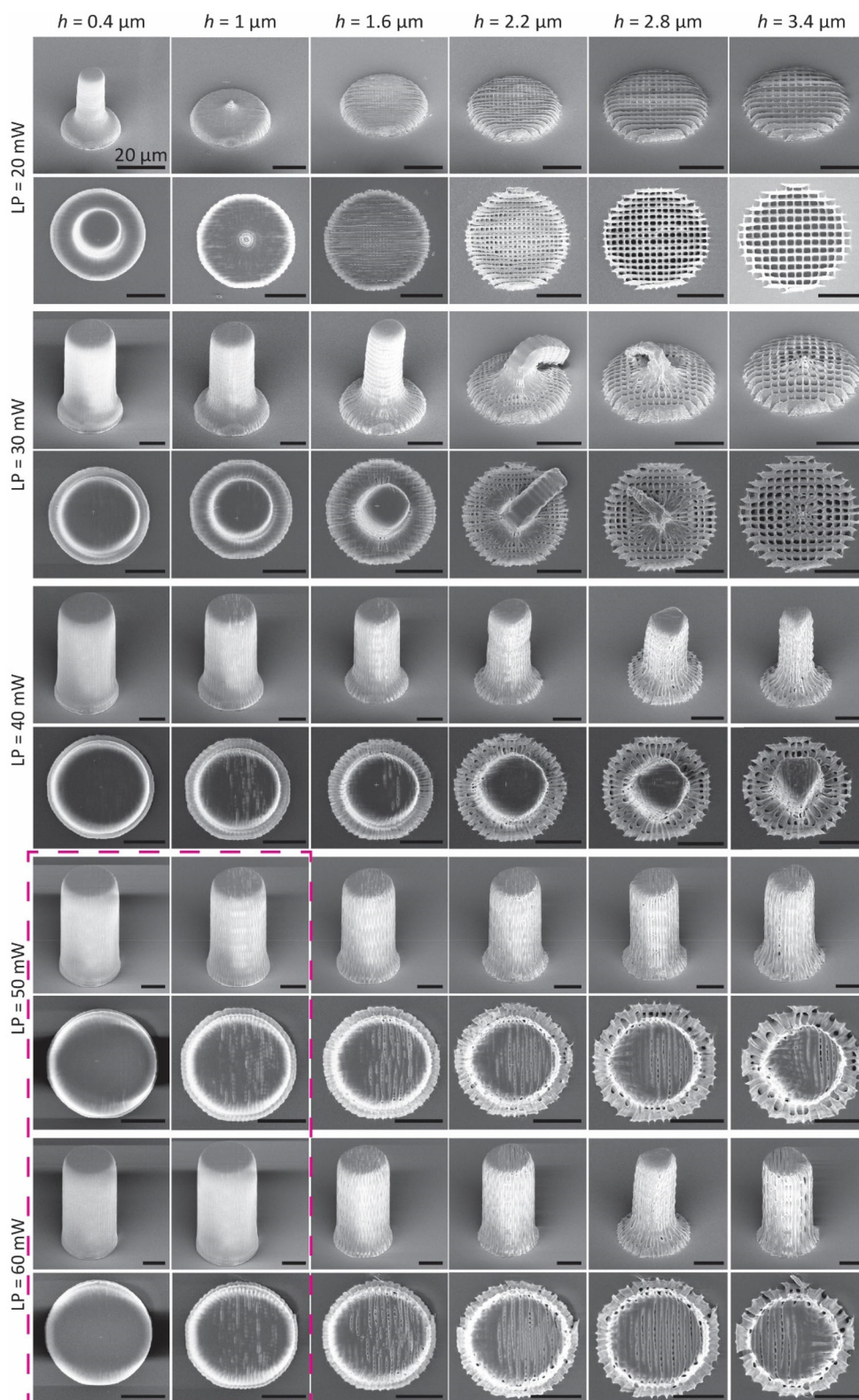


**Figure 5.** Top and tilt-view (52°) SEM images of 2PP-printed IP-Q micropillars fabricated with varying hatching distance ( $h = 0.4\text{--}3.4\ \mu\text{m}$ ) and laser power ( $LP = 40\text{--}120\%$ ) for constant slicing distance ( $s = 5\ \mu\text{m}$ ) and scanning speed ( $v = 100\ \text{mm s}^{-1}$ ) (scale bar =  $20\ \mu\text{m}$ ). The dashed lines enclose the highest-quality prints.

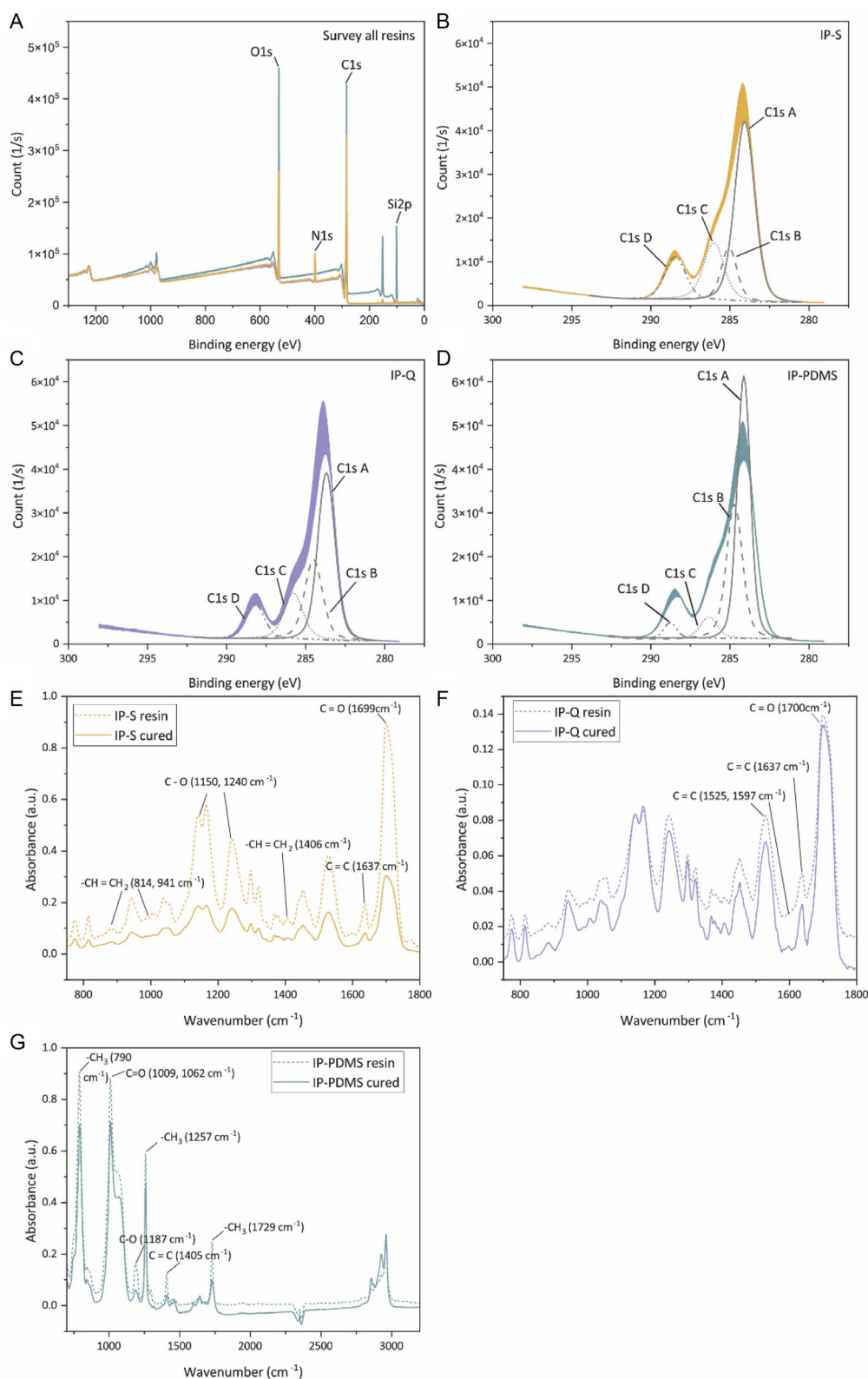


**Figure 6.** A) XPS survey spectra for IP-S, IP-Q, and IP-PDMS Nanoscribe resins. High energy resolution XPS spectrum of C1s region on B) IP-S, C) IP-Q, and D) IP-PDMS samples. The FTIR spectra of the E) IP-S resin (dashed line) and the cured version (solid line), F) IP-Q resin (solid line) and the cured version (dashed line), and G) IP-PDMS resin (solid line) and the cured version (dashed line).

**Table 3.** The binding energy and atomic percentage of the C1s, O1s, Si2p, and N1s regions for the IP-S, IP-Q, and IP-PDMS Nanoscribe resins.

Bond type	IP-S		IP-Q		IP-PDMS	
	Binding energy [eV]	Atomic percentage [%]	Binding energy [eV]	Atomic percentage [%]	Binding energy [eV]	Atomic percentage [%]
C 1s	284.47	71.93	284.10	75.26	284.05	57.42
C1s A (C—C)	284.07	39.18	283.69	34.89	283.48	25.10
C1s B (C—O)	285.06	9.39	284.51	18.18	284.07	16.38
C1s C (O—C=O)	286.02	13.48	285.78	11.15	285.69	2.77
C1s D (C=O)	288.46	9.66	288.22	8.06	288.13	1.55
O 1s	532.15	21.25	531.87	19.29	531.56	22.89
O1s A	531.20	10.26	531.04	11.00	530.99	17.54
O1s B	532.77	11.40	532.58	8.24	532.29	2.20
Si 2p	101.43	1.43	101.22	4.45	101.42	19.33
Si2p3 A	101.24	1.01	100.96	2.01	100.72	17.09
Si2p1 A	101.97	0	101.69	2.01	101.42	17.10
N 1s	399.34	5.40	394.56	1.00	399.23	0.37
N1s A	399.20	5.62	398.94	4.47	398.66	0.28

at 284.05 eV (Figure 6D). A peak deconvolution for each of the resins confirms the presence of C—C (C1s A), C—O (C1s B), O—C=O (C1s C), and C=O (C1s D) groups. The corresponding binding energies are listed in Table 3. Due to polymerization, the resins' FTIR spectra indicated the depleted bonds' positions. For IP-S, the depletion of the characteristic bands associated with the C=C group was found at 814, 941, 1406, and 1637 cm<sup>-1</sup> (Table S7–S8, Supporting Information). The corresponding values for C=O and C—O were at 1699 and 1150/1240 cm<sup>-1</sup>. According to Equation (1), the DC, based on the decrease in height at 1637 cm<sup>-1</sup>, was ≈61% (Table S9, Supporting Information). The depletion of the C=C groups at 1525, 1597, and 1639 cm<sup>-1</sup>, and the C=O group at 1700 cm<sup>-1</sup>, corroborate the polymerization of the IP-Q resin, with an approximate DC of 38% based on the peak height change at 1639 cm<sup>-1</sup> (Table S7–S9, Supporting Information). The polymerization of IP-PDMS can be confirmed by the decrease of the intensity of different functional groups at 790, 1257, and 1729 cm<sup>-1</sup>, related to the Si—CH<sub>3</sub> group, at 1009 and 1062 cm<sup>-1</sup>, related to the C=O group, at 1187 cm<sup>-1</sup> because of the C—O group, and at 1405 cm<sup>-1</sup> related to the C=C group, that yield an approximate DC = 61% at that wavenumber (Table S7–S9, Supporting Information).

### 3.4. Mechanical Characterization of Microscale Structures and Micropillars

The stiffness values of the solid and porous structures, made from IP-Q and IP-S resins, were within the same range: 32.97 ± 0.16 kN m<sup>-1</sup> and 33.77 ± 0.28 kN m<sup>-1</sup> for the solid versions and 27.91 ± 0.06 kN m<sup>-1</sup> and 26.98 ± 0.19 kN m<sup>-1</sup> for the porous versions, respectively (Figure 7A). The porous structures exhibited ≈85% (IP-Q) and 80% (IP-S) of the stiffness of their solid counterparts. The solid IP-PDMS structures had a stiffness of 11.8 ± 0.1 N m<sup>-1</sup>, and the porous ones had a stiffness of 5.80 ± 0.4 N m<sup>-1</sup>. Thus, they had a stiffness ≈50% smaller than

that of their solid counterparts (Figure 7B). The difference in the stiffness of solid and porous structures made for each resin type was statistically significant (Table S1, Supporting Information). Cross-material comparison with ANOVA (Table S2, Supporting Information) and the post-hoc Tukey's test (Table S3, Supporting Information) allow for a deeper assessment of cross-material comparison. Within each material, significant differences were found between solid and porous structures, confirming the expected reduction in stiffness with the introduction of porosity (IP-Q:  $p = 0.0008$ ; IP-S:  $p < 0.0001$ ; IP-PDMS:  $p < 0.0001$ ). When comparing across materials, both solid and porous IP-Q and IP-S exhibited comparable stiffness values, with no statistically significant differences detected. By contrast, IP-PDMS structures were consistently and significantly less stiff than both IP-Q and IP-S, regardless of whether solid or porous architectures were compared ( $p < 0.0001$ ). These findings indicate that, while porosity reduces stiffness within each resin system, the cross-material comparison confirms the hierarchy of mechanical performance with IP-Q and IP-S behaving similarly and IP-PDMS being significantly more compliant.

The elastic modulus  $E$  was calculated for the solid structures based on Equation (2)

$$E = k \times L/A \quad (2)$$

where  $k$  is the measured stiffness of the solid structure,  $L$  is the length of the cylindrical tip of the microstructure, and  $A$  is the surface area of the cylindrical tip (Table S4, Supporting Information). The calculated elastic moduli were 2.04 GPa for IP-Q, 2.03 GPa for IP-S, and 870 MPa for IP-PDMS.

The mechanical properties of the IP-Q micropillars,  $E$ , and  $\sigma_y$ , displayed a distinct dependence on the 2PP printing parameters. For LP = 20 and 30 mW, the micropillars were either not printed or lacked stability, preventing mechanical characterization (Figure 3 and 5). In general,  $E$  and  $\sigma_y$  increased with larger LP values but decreased with increasing  $h$  and  $s$  values. The range of Young's moduli achieved was  $E = 1.31$ – $3.7$  GPa, while the

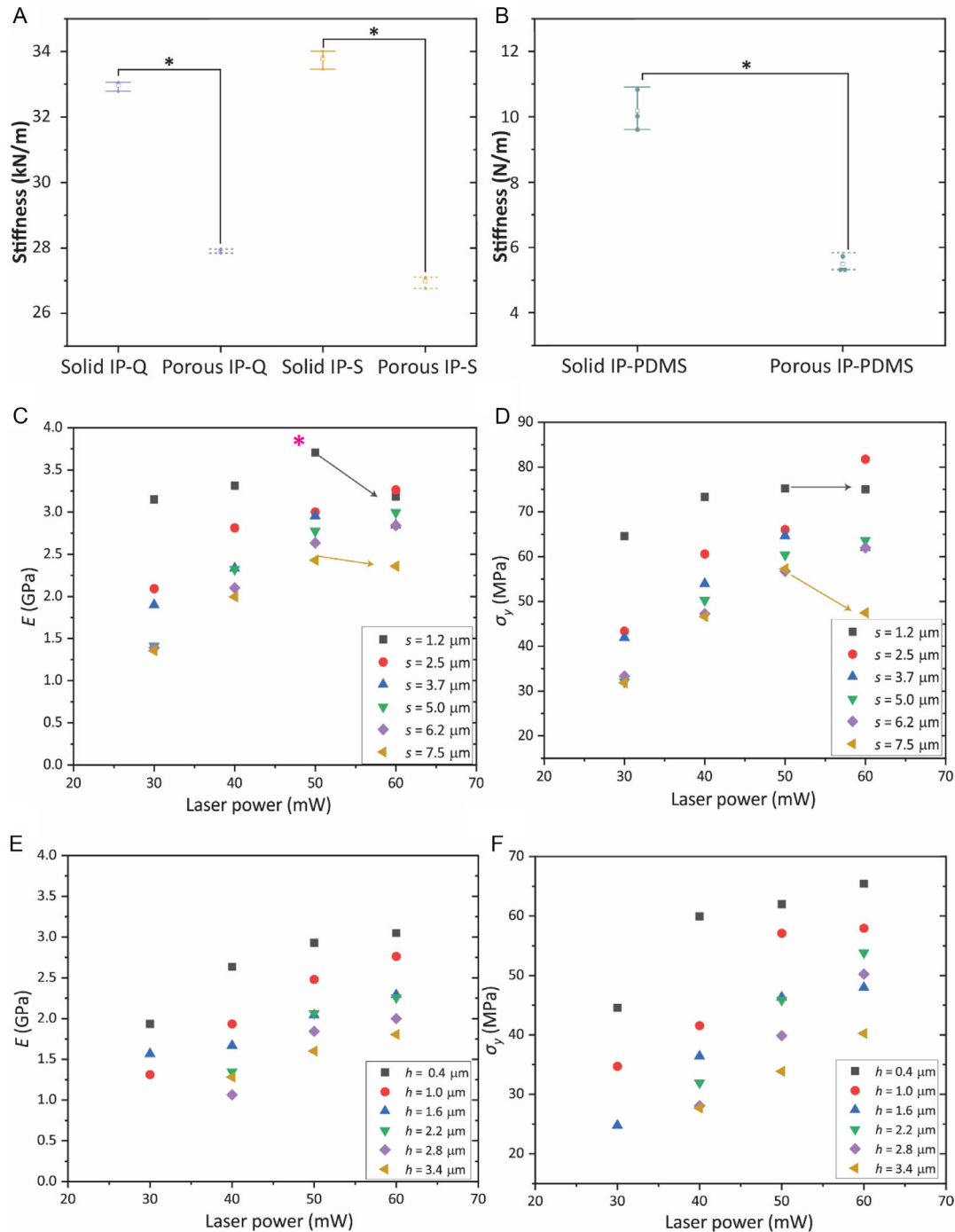


**Figure 7.** The box plots for the stiffness values of solid and porous microstructures printed with A) IP-Q and IP-S and B) IP-PDMS. Relationships between laser power (LP), slicing distance (s), hatching distance (h), and the resultant mechanical properties, E modulus, and yield stress  $\sigma_y$  of micropillars fabricated using IP-Q. C) E (\* highest value achieved) and D)  $\sigma_y$  for  $h = 1 \mu\text{m}$ ,  $s = 1.2\text{--}7.5 \mu\text{m}$  and LP = 30–60 mW, E) E, and F)  $\sigma_y$  for  $s = 5 \mu\text{m}$ ,  $h = 0.4\text{--}3.4 \mu\text{m}$ , and LP = 30–60 mW.

yield strength ranged  $\sigma_y = 24.77\text{--}81.75 \text{ MPa}$ . The best mechanical properties were achieved for LP = 50 mW,  $h = 1 \mu\text{m}$ , and  $s = 1.2 \mu\text{m}$  and were  $E = 3.7 \text{ GPa}$  and  $\sigma_y = 75.21 \text{ MPa}$  (Figure 7C,D). Interestingly, the highest E and  $\sigma_y$  values were not associated with the largest achieved dimensions, D and H.

For LP = 60 mW, E decreased to 3.2 GPa, but the yield strength value ( $\sigma_y = 75.05 \text{ MPa}$ ) remained similar to the value obtained at LP = 50 mW (Figure 7C,D). For LP = 50 mW,  $h = 1 \mu\text{m}$ , and  $s = 7.5 \mu\text{m}$ , the resulting micropillars exhibited  $E = 2.4 \text{ GPa}$  and  $\sigma_y = 57.3 \text{ MPa}$ . Increasing the LP to 60 mW (keeping



$h = 1 \mu\text{m}$  and  $s = 7.5 \mu\text{m}$ ) resulted in a slight reduction to  $E = 2.36 \text{ GPa}$ , which is almost comparable to the previous value (Figure 7C). The yield strength, however, decreased by nearly 20%, dropping to  $\sigma_y = 47.5 \text{ MPa}$  (Figure 7D). This indicates that while the  $E$  remains relatively unaffected by the increase in LP, the  $\sigma_y$  is adversely impacted, highlighting a trade-off between these mechanical properties at higher LP settings. For varying  $h$  distances, the mechanical properties of the micropillars followed the general rule of increasing values with increasing LP values (Figure 7E,F).

## 4. Discussion

We aimed to understand the effects of the different parameters of the 2PP printing method on the shape fidelity and mechanical properties of microscale solid and porous structures fabricated from various resins. Therefore, we printed solid and porous microscale structures using the commercial materials IP-Q, IP-S, and IP-PDMS and characterized them morphologically, chemically, and mechanically. This comprehensive study, the most detailed yet available in the literature, enables a better understanding of the process–structure (morphology and chemistry)–mechanics relationships relevant to 2PP technology, especially considering that IP-Q has not been extensively investigated.

### 4.1. Stiffness Retention in Porous Microscale Structures

The stiffness and calculated elastic moduli of the solid and porous structures in this study were evaluated and compared with available literature data. The solid structures made from IP-Q and IP-S resins exhibited calculated elastic moduli of 2.04 and 2.03 GPa, respectively. These values are lower than the reported elastic moduli for these resins (3.17 GPa<sup>[11]</sup> for IP-Q and 4.6 GPa<sup>[15]</sup> for IP-S). For IP-PDMS, the calculated elastic modulus of 870 MPa is significantly higher than the 17.8 MPa value reported in the literature.<sup>[16]</sup> These discrepancies can be attributed to differences in the printing parameters, the scale of the tested structures, and the mechanical testing method applied.

In terms of stiffness, the solid IP-Q and IP-S structures demonstrated comparable values, consistent with their similar elastic moduli, and the porous structures retained 80%–85% of the stiffness of the solid ones. For IP-PDMS, the porous structures retained only half the stiffness of the solid counterparts, highlighting the material's inherently compliant character. The results show that the mechanical properties of 2PP-fabricated solid microstructures differ from bulk material properties reported in the literature, emphasizing the critical influence of microfabrication parameters, sample design, and testing methods on the evaluation of mechanical performance. This is in accordance with the literature on woodpile structures that have exhibited mechanical response similar to foams and lattices and thus have proven to be able to modulate the elastic performance by tuning the density of the structure.<sup>[29]</sup>

The SEM/FIB images of the cross-section morphology of the porous microstructures made of the three materials revealed well-defined pores in all the samples (Figure 2). However, accurately evaluating the pore size of the microstructures was

challenging. The SEM/FIB imaging proved unreliable for measuring the pore size, as the ablation process can often introduce artifacts and deformations in the cross-section.<sup>[30]</sup> X-ray micro-CT was also explored but deemed unsuitable because the printing resolution of the structures approached the imaging resolution of the available devices.

Therefore, to estimate the porosity range of the printed microstructures, we applied the Gibson–Ashby model,<sup>[31]</sup> using the stiffness values obtained from the micromechanical tests. According to this model, a power-law relationship exists between the relative density of a porous structure and its mechanical properties

$$k^*/k_{\text{solid}} = C \times (\rho^*/\rho_{\text{solid}})^n \quad (3)$$

where  $k^*$  and  $k_{\text{solid}}$  represent the stiffness of the porous and solid structures, respectively,  $\rho^*$  and  $\rho_{\text{solid}}$  are their corresponding densities,  $C$  is the Gibson–Ashby constant, and  $n$  is a material-specific exponent.

For this analysis, we assumed  $C = 1$  and  $n = 1$  and 2. Using these assumptions, we calculated the range of the relative density ( $\rho^*/\rho_{\text{solid}}$ ) and porosity ( $\varphi$ ) for the three investigated microstructures (Table 4). Based on these calculations, the porosity values of the samples were estimated to be between 8.5% ( $n = 1$ ) to 15.5% ( $n = 2$ ) for IP-Q, between 15.5% ( $n = 1$ ) to 20% ( $n = 2$ ) for IP-S and between 31.5% ( $n = 1$ ) and 51% ( $n = 2$ ) for IP-PDMS.

The Gibson–Ashby model results deviate significantly from the designed porosity of 26% for all structures (Table S5, Supporting Information). For IP-Q and IP-S, the estimated porosity values are lower than the design, which can be attributed to partial pore closure and reduced pore connectivity during the 2PP fabrication process. Several factors may explain these discrepancies. First, the DC in 2PP resins is typically incomplete, as also observed in this study, leading to local variations in cross-link density and densification of the polymer network, which effectively reduces the available pore volume. Second, voxel size, overlap, and local laser intensity influence the exposure dose,<sup>[32–34]</sup> while increased overlap can counterbalance insufficient conversion, excessive exposure may cause material accumulation that narrows or even closes the designed pores. Third, postprocessing steps introduce additional variation, as capillary forces during solvent evaporation and the release of internal stresses can promote shrinkage or deformation of thin

**Table 4.** Calculated relative density ( $\rho^*/\rho_{\text{solid}}$ ) for IP-Q, IP-S, and IP-PDMS samples based on the Gibson–Ashby model. The minimum and maximum relative density and porosity ( $\varphi$ ) for two values of the material-specific exponent ( $n = 1$ ,  $n = 2$ ) are presented for each case. Average porosity ( $\varphi$ ) in percentage for the different  $n$  values and the designed porosity ( $\varphi_{\text{theoretical}}$ ).

Material	Exponent $n$	Min $\rho^*/\rho_{\text{solid}}$	Max $\rho^*/\rho_{\text{solid}}$	$\varphi$ [%]	$\varphi_{\text{theoretical}}$ [%]
IP-Q	1	0.84	0.85	15.5	26
	2	0.91	0.92	8.5	
IP-S	1	0.79	0.81	20	10.5
	2	0.89	0.90	10.5	
IP-PDMS	1	0.45	0.53	51	31.5
	2	0.67	0.73	31.5	

features.<sup>[35]</sup> In contrast, the higher porosity values estimated for IP-PDMS suggest that its printed pore size and connectivity were closer to the design, as also supported by SEM/FIB imaging. When comparing the three resins, it becomes evident that printing the same porous design requires very different compromises in processing. This comparison highlights how delicate and resin-specific the optimization of printing parameters must be in order to balance polymerization kinetics, voxel geometry, and development effects to achieve reliable porosity across different materials.

To validate theoretical models like Gibson–Ashby, future studies could incorporate FEA simulations to model the deformation and mechanical properties of the porous structures more effectively. Submicron X-ray imaging, potentially combined with in situ mechanical testing and digital image correlation techniques, could provide accurate, high-resolution validation of both porous structures, and FEA models. Moreover, this study did not investigate orientation-dependent effects, as all structures were printed vertically. Since build angle can influence voxel arrangement, polymerization efficiency, and material anisotropy, it is expected to affect both geometry and mechanical properties. Printing orientation therefore represents an unexplored parameter that should be systematically studied in future work, particularly for porous architectures and large aspect ratio structures.

A key novelty of this study lies in the direct comparison of stiffness retention across three different materials—IP-Q, IP-S, and IP-PDMS—fabricated into similar porous designs. By employing the same geometric design and fabrication process, this approach reveals how each resin responds to the introduction of porosity. Such a comparative analysis is not reported in the literature and provides unique insights into material-specific behaviors, such as stiffness retention and porosity influence, under identical experimental conditions. Recent work has demonstrated that 2PP-fabricated microstructured arrays can guide neuronal outgrowth by tailoring mechanical stiffness and topographical cues.<sup>[36]</sup> These findings further support the potential of finely tuned 2PP architectures across scales and materials in the tissue engineering field.

#### 4.2. The Influence of the Printing Parameters on the Morphology and Mechanical Properties of the IP-Q Micropillars

Our investigation into the impact of the 2PP printing parameters on micropillar fabrication revealed the effects of various printing parameters (e.g., LP,  $h$ ,  $s$ ) on their morphology and their mechanical properties. Higher LP generally resulted in a larger diameter and larger micropillar height, confirming that greater energy input leads to sufficient polymerization and more robust structures.<sup>[9,32,37,38]</sup> The printing parameters  $h$  and  $s$  exhibited an inverse relationship with the apparent geometry. Increased  $h$  and  $s$  reduced both the diameter and the height of the pillars. This can be explained by the fact that reduced exposure of the material to the laser results in less crosslinking and sparse structures. Increasing the LP generally had a positive effect in reducing the impact of the slicing and hatching distances on the diameter, height, and mechanical properties of the fabricated micropillars.<sup>[38]</sup> The desired micropillar geometry, however, was not achieved with any of the tested parameter combinations,

highlighting the need for design adjustments. On average, the lateral dimension (diameter) should be increased by  $\approx 30\%$ , while the axial dimension (height) should be reduced by about 10% to achieve the target geometry under most tested conditions. The decrease in both diameter and height for  $h = 2.8 \mu\text{m}$  and  $s = 5 \mu\text{m}$  despite the large LP = 60 mW shows that there is a boundary to the extent the LP can positively contribute to a better geometry. That is because excessive LP can cause a saturation in the polymerization of the material and induce burning. The morphological trends were to a large extent similar to the results of the mechanical properties of the micropillars. In most cases, both the elastic modulus and the yield strength of the micropillars increased with an increasing LP and for small  $h$  and  $s$  values. The reduction in mechanical performance observed at 60 mW can be attributed to overexposure effects in 2PP. At such high intensities, the polymerization process no longer scales linearly with energy input, as photoinitiator saturation and radical recombination limit effective crosslinking, while local heating at the focal region can introduce residual stresses or even partial degradation of the polymer matrix. Similar dose-saturation and thermal degradation phenomena have been reported in nonlinear photopolymerization systems.<sup>[37,39,40]</sup> These mechanisms explain why the elastic modulus increased up to 50 mW but plateaued or decreased at higher powers, suggesting that an optimal LP window exists for IP-Q. The best mechanical properties ( $E = 3.7 \text{ GPa}$ ,  $\sigma_y = 75.21 \text{ MPa}$ ) were, however, not achieved for LP = 60 mW but for LP = 50 mW and the smallest slicing distance ( $s = 1.2 \mu\text{m}$ ). The calculation of the DC = 37% for those conditions confirmed an efficient exposure of the material to the LP. Unlike prior work,<sup>[11]</sup> where the  $E$  values of the 2PP-printed IP-Q samples were assessed by using indentation testing, we employed uniaxial micropillar compression to evaluate the mechanical properties. The  $E$  values measured in our study are notably larger and this can be attributed to the hatching and slicing parameters that are much smaller than the values explored before and can lead to higher structural density. Another aspect that can explain the differences in the measured values is the presence of surface imperfections and heterogeneities, which can affect the indentation results. In contrast, the micropillar compression approach provides an evaluation of the bulk mechanical properties. Moreover, the DC value obtained for IP-Q in this study is also smaller than the already reported one. The reported values were between 55% and 80%. However, the spectra were obtained with Raman spectroscopy, and the DC calculation was performed by inspecting the changes in the area below the relevant peak, while we obtained the data with FTIR spectroscopy and calculated the value by looking at differences in the peak height.

#### 4.3. Influence of Physical Exposure Parameters on Polymerization, Mechanics and Suitability for Biomedical Applications

To better interpret the structure–property relationships, we further calculated the physical exposure parameters associated with the 2PP process following frameworks proposed in recent literature on nonlinear photopolymerization systems.<sup>[41,42]</sup> These include intensity ( $I$ ), fluence per pulse ( $F_p$ ), exposure dose ( $D$ ),

number of pulses per voxel, voxel overlap ( $\delta$ ), focal spot geometry (lateral diameter,  $d_{xy}$ , Rayleigh length,  $z_R$ ) derived from the system's optical configuration parameters ( $\lambda$ , NA,  $f$ ,  $\tau$ ), and the chosen printing parameters (LP,  $v$ ,  $h$ ,  $s$ ) (Table S10–S12, Supporting Information).

For the fabricated microstructures, the voxel lateral diameter and Rayleigh length spanned  $\approx 3.17$  and  $10.13 \mu\text{m}$  for IP-Q,  $\approx 1.19$  and  $1.42 \mu\text{m}$  for IP-S and IP-PDMS, with voxel overlaps ( $\delta$ ) being 0.92, 0.72, and 0.48, respectively. These values show that tighter focusing and a voxel overlap of  $\approx 50\%$  were sufficient to achieve stable structures with IP-PDMS. For IP-S that exhibits the same focal geometry as IP-PDMS but with larger voxel overlap, and for IP-Q that exhibits the largest focal geometry and the largest overlap, we also observe the most significant retention in the mechanical properties compared to IP-PDMS.

We also evaluated the physical exposure parameters for the micropillars fabricated with IP-Q under varying hatching and slicing distances. In both cases (constant  $h$  or  $s$ ), increasing LP resulted in systematically higher fluence and dose. Interestingly, when slicing was fixed and hatching varied, the voxel overlap even reached negative values (indicating no voxel overlap), and aligned well with the less dense structures observed (Figure 5).

The relationship between mechanical performance and the peak intensity calculated for the printing of microstructures across all three IP resins revealed a consistent sublinear scaling of both Young's modulus ( $E$ ) and yield strength ( $\sigma_y$ ) across all tested micropillars made from IP-Q (Figure S2, Supporting Information). The power-law fitting yielded exponents ( $\beta$ ) ranging from 0.08 to 1.41, significantly below the quadratic behavior expected for ideal two-photon absorption. These results corroborate previous observations that reported saturation-like deviations from ideal quadratic two-photon behavior in different photopolymer systems.<sup>[41,43]</sup>

The calculated exposure intensities in this study,  $6.33 \times 10^{-10}$ – $1.12 \times 10^{-12} \text{ W cm}^{-2}$ , appear to be in the range but slightly lower than those reported in the literature for initiator-free systems ( $0.58$ – $1.55 \times 10^{-12} \text{ W cm}^{-2}$ ).<sup>[44]</sup> Moreover, the influence of reflective silicon substrates was not considered in the selection of printing parameters. However, periodic interference and standing wave effects may locally affect the exposure, the crosslinking, and explain the ridge-like structures on all 2PP printed structures (Figure 2, 3, and 5).<sup>[41]</sup>

In addition to optical exposure parameters, thermal effects during printing and post-curing have also been shown to influence geometry and mechanical performance of 2PP structures. Specifically, thermal control during printing can improve the resolution of lattice structures,<sup>[45]</sup> while thermal postcuring has been reported to increase the DC and enhance the mechanical properties of 2PP printed structures.<sup>[46]</sup> In the present study, thermal effects could not be investigated with our in-house system, and we focused exclusively on as-printed samples. Future work should therefore explore thermal management strategies, both during fabrication and in postprocessing, to further harness the process–structure–property regime of IP resins.

Another crucial aspect of these resins is their suitability for biomedical application. The IP resins investigated here (IP-Q, IP-S, and IP-PDMS) are crosslinked thermosets, which are inherently resistant to hydrolysis and therefore not expected to degrade under physiological humidity and temperature ( $\approx 37^\circ\text{C}$ ).

According to the manufacturer thermal softening occurs only above  $\approx 55^\circ\text{C}$ , outside the range relevant for implantation. These considerations were among the reasons for selecting these resins; however, systematic studies of long-term degradation and stability in biologically relevant environments remain necessary. Previous reports, however, have demonstrated favorable cytocompatibility for IP resins used in 2PP,<sup>[14,47–50]</sup> supporting their potential for biomedical applications. Nevertheless, future studies should perform in-depth evaluations of the biological response on the specific porous and solid architectures presented in this study to confirm their suitability for biomedical translation.

## 5. Conclusion

This study demonstrates how 2PP printing parameters govern the morphology and mechanical properties of microscale solid and porous structures fabricated from IP-Q, IP-S, and IP-PDMS resins. For all resins, a set of printing conditions was identified that enabled reproducible structures with morphological integrity. The differences in the optimum printing conditions were attributed to variations in the polymerization behavior of the resins. IP-Q and IP-S required smaller hatching and slicing distances, along with lower LP, to achieve reliable printing of the structures. In contrast, IP-PDMS needed higher LP and larger hatching distance for effective polymerization and structural integrity.

Mechanical characterization further revealed material-dependent differences. The porous microstructures made from IP-Q and IP-S resins retained 85% of the stiffness of their solid versions, while the IP-PDMS porous microstructures retained only 50% of the stiffness of their solid counterparts, likely due to the inherently more compliant nature of the IP-PDMS material.

For IP-Q micropillars, reducing slicing and hatching distances improved dimensional fidelity, while increasing LP up to 50 mW enhanced mechanical properties. However, excessive exposure introduced geometrical aberrations and reduced yield strength, underscoring the trade-off between accuracy and mechanical performance.

Overall, this work establishes a systematic framework for understanding how 2PP processing parameters affect the manufacturability, geometry, and micromechanical behavior of commercial resins. These insights provide a foundation for future studies, where device-specific mechanical performance requirements, such as those of cochlear implants, can be directly addressed.

## Supporting Information

Supporting Information is available from the Wiley Online Library or from the author.

## Acknowledgements

A.I. and M.G. contributed equally to this work. This project has received funding from the Interreg 2 Seas program 2014–2020, cofunded by the European Regional Development Fund under subsidy contract “Site Drug 2S07-033”.

## Conflict of Interest

The authors declare no conflict of interest.

## Data Availability Statement

The data that support the findings of this study are available from the corresponding author upon reasonable request.

## Keywords

IP-PDMS, IP-Q, IP-S, multiscale structures micromechanics, two-photon polymerization

Received: July 5, 2025  
Revised: August 30, 2025  
Published online:

- [1] X. Jing, H. Fu, B. Yu, M. Sun, L. Wang, *Front. Bioeng. Biotechnol.* **2022**, 10, 994355.
- [2] M. T. Raimondi, S. M. Eaton, M. M. Nava, M. Laganà, G. Cerullo, R. Osellame, *J. Appl. Biomater. Funct. Mater.* **2012**, 10, 56.
- [3] C. Greant, B. Van Durme, J. Van Hoorick, S. Van Vlierberghe, *Adv. Funct. Mater.* **2023**, 33, 2212641.
- [4] A. Ovsianikov, A. Doraiswamy, R. Narayan, B. N. Chichkov, Two-photon polymerization for fabrication of biomedical devices, in *Microfluidics, BioMEMS, and Medical Microsystems V*, SPIE **2007**, p. 64650O.
- [5] C. Liao, A. Wuethrich, M. Trau, *Appl. Mater. Today* **2020**, 19, 100635.
- [6] J. R. Thompson, K. S. Worthington, B. J. Green, N. K. Mullin, C. Jiao, E. E. Kaalberg, L. A. Wiley, I. C. Han, S. R. Russell, E. H. Sohn, C. A. Guymon, R. F. Mullins, E. M. Stone, B. A. Tucker, *Acta Biomater.* **2019**, 94, 204.
- [7] P. Timashev, D. Kuznetsova, A. Koroleva, N. Prodanets, A. Deiwick, Y. Piskun, K. Bardakova, N. Dzhyoyashvili, S. Kostjuk, E. Zagaynova, Y. Rochev, B. Chichkov, V. Bagratashvili, *Nanomedicine* **2016**, 11, 1041.
- [8] C. LaFratta, T. Baldacchini, *Micromachines* **2017**, 8, 101.
- [9] P. F. J. van Altena, A. Accardo, *Polymers* **2023**, 15, 1816.
- [10] L. Angeloni, M. Ganjian, M. Nouri-Goushki, M. J. Mirzaali, C. W. Hagen, A. A. Zadpoor, L. E. Fratila-Apachitei, M. K. Ghatkesar, *Addit. Manuf.* **2021**, 39, 101858.
- [11] S. Schweiger, T. Schulze, S. Schlipf, P. Reinig, H. Schenk, *J. Opt. Microsyst.* **2022**, 2, 33501.
- [12] F. Zurita, L. Grob, A. Erben, F. Del Duca, H. Clausen-Schaumann, S. Sudhop, O. Hayden, B. Wolfrum, *Adv. Mater. Technol.* **2023**, 8, 2200989.
- [13] L. Jonušauskas, D. Gailevičius, S. Rekštytė, T. Baldacchini, S. Juodkakis, M. Malinauskas, *Opt. Express* **2019**, 27, 15205.
- [14] A. Isaakidou, I. Apachitei, L. E. Fratila-Apachitei, A. A. Zadpoor, *J. Funct. Biomater.* **2023**, 14, 494.
- [15] R. C. L. N. Kramer, E. J. Verlinden, L. Angeloni, A. van den Heuvel, L. E. Fratila-Apachitei, S. M. van der Maarel, M. K. Ghatkesar, *Lab Chip* **2020**, 20, 311.
- [16] A.-I. Bunea, N. d. C. Iniesta, A. Droumpali, A. E. Wetzels, E. Engay, R. Taboryski, *Micro* **2021**, 1, 164.
- [17] M. Oellers, F. Lucklum, M. J. Vellekoop, *Microfluid. Nanofluid.* **2020**, 24, 4.
- [18] E. Fakeih, A. A. Aguirre-Pablo, S. T. Thoroddsen, K. N. Salama, *Adv. Eng. Mater.* **2023**, 25, 2300161.
- [19] A. S. Cordeiro, I. A. Tekko, M. H. Jomaa, L. Vora, E. McAlister, F. Volpe-Zanutto, M. Nethery, P. T. Baine, N. Mitchell, D. W. McNeill, R. F. Donnelly, *Pharm. Res.* **2020**, 37, 174.
- [20] S. Mckee, A. Lutey, C. Sciancalepore, F. Poli, S. Selli, A. Cucinotta, *J. Photochem. Photobiol. B* **2022**, 229, 112424.
- [21] S. Czich, T. Wloka, H. Rothe, J. Rost, F. Penzold, M. Kleinstaub, M. Gottschaldt, U. S. Schubert, K. Liefeth, *Molecules* **2020**, 25, 5066.
- [22] Y. Yuan, L. Chen, Z. Shi, J. Chen, *Nanomaterials* **2022**, 12, 391.
- [23] E. Juère, R. Caillard, F. Kleitz, *Microporous Mesoporous Mater.* **2020**, 306, 110482.
- [24] J. Parra-Nieto, M. A. G. del Cid, I. A. de Cárcer, A. Baeza, *Biotechnol. J.* **2021**, 16, 2000150.
- [25] A. Isaakidou, M. Ganjian, R. van Hoften, M. C. Saldivar, M. A. Leeflang, A. Groetsch, M. Wątroba, J. Schwiedrzik, M. J. Mirzaali, I. Apachitei, L. E. Fratila-Apachitei, A. A. Zadpoor, *Front. Bioeng. Biotechnol.* **2024**, 11, 1289299.
- [26] G. Rochat, Y. Leterrier, P. Fayet, J.-A. E. Månson, *Thin Solid Films* **2003**, 437, 204.
- [27] M. Kwaśny, A. Bombalska, K. Obroniecka, *Sensors* **2022**, 22, 2170.
- [28] J. Pyszkowski, K. Bielawski, Piuma Nanoindenter - User Manual, Optics11 **2019**, www.optics11.com.
- [29] S. Juodkakis, V. Mizeikis, K. K. Seet, H. Misawa, U. G. K. Wegst, *Appl. Phys. Lett.* **2007**, 91, 241904.
- [30] A. G. Clark, R. Wang, Y. Qin, Y. Wang, A. Zhu, J. Lomeo, Q. Bao, D. J. Burgess, J. Chen, B. Qin, Y. Zou, S. Zhang, *J. Controlled Release* **2022**, 349, 580.
- [31] T. Maconachie, R. Tino, B. Lozanovski, M. Watson, A. Jones, C. Pandelidi, A. Alghamdi, A. Almalki, D. Downing, M. Brandt, M. Leary, *Int. J. Adv. Manuf. Technol.* **2020**, 107, 4449.
- [32] E. D. Lemma, F. Rizzi, T. Dattoma, B. Spagnolo, L. Sileo, A. Qualtieri, M. De Vittorio, F. Pisanello, *IEEE Trans. Nanotechnol.* **2016**, 16, 23.
- [33] H. Wang, C.-F. Pan, C. Li, K. S. Menghrajani, M. A. Schmidt, A. Li, F. Fan, Y. Zhou, W. Zhang, H. Wang, P. N. S. Nair, J. Y. E. Chan, T. Mori, Y. Hu, G. Hu, S. A. Maier, H. Ren, H. Duan, J. K. W. Yang, *Int. J. Extreme Manuf.* **2024**, 6, 042002.
- [34] J. Bauer, A. G. Izard, Y. Zhang, T. Baldacchini, L. Valdevit, *Adv. Mater. Technol.* **2019**, 4, 1900146.
- [35] J. Purtov, A. Verch, P. Rogin, R. Hensel, *Microelectron. Eng.* **2018**, 194, 45.
- [36] G. Flamourakis, Q. Dong, D. Kromm, S. Teurlings, J. van Haren, T. Allert, H. Smeenk, F. M. S. de Vrij, R. P. Tas, C. S. Smith, D. Brinks, A. Accardo, *Adv. Funct. Mater.* **2025**, 35, 2409451.
- [37] C.-S. Shin, T.-J. Li, C.-L. Lin, *Micromachines* **2018**, 9, 615.
- [38] M. Diamantopoulou, N. Karathanasopoulos, D. Mohr, *Addit. Manuf.* **2021**, 47, 102266.
- [39] Q. Hu, G. A. Rance, G. F. Trindade, D. Pervan, L. Jiang, A. Foerster, L. Turyanska, C. Tuck, D. J. Irvine, R. Hague, R. D. Wildman, *Addit. Manuf.* **2022**, 51, 102575.
- [40] E. Sedghamiz, M. Liu, W. Wenzel, *Nat. Commun.* **2022**, 13, 2115.
- [41] H. Wang, W. Zhang, D. Ladika, H. Yu, D. Gailevičius, H. Wang, C. Pan, P. N. S. Nair, Y. Ke, T. Mori, J. Y. E. Chan, Q. Ruan, M. Farsari, M. Malinauskas, S. Juodkakis, M. Gu, J. K. W. Yang, *Adv. Funct. Mater.* **2023**, 33, 2214211.
- [42] X. Zhou, Y. Hou, J. Lin, *AIP Adv.* **2015**, 5, 030701.
- [43] R. Cunha, J. V. P. Valverde, L. De Boni, L. Misoguti, C. R. Mendonça, *ACS Omega* **2025**, 10, 1440.
- [44] D. Ladika, A. Butkus, V. Melissinaki, E. Skliutas, E. Kabouraki, S. Juodkakis, M. Farsari, M. Malinauskas, *Light: Adv. Manuf.* **2024**, 5, 567.
- [45] K. Takada, K. Kaneko, Y.-D. Li, S. Kawata, Q.-D. Chen, H.-B. Sun, *Appl. Phys. Lett.* **2008**, 92, 041902.



- [46] J. Bauer, A. G. Izard, Y. Zhang, T. Baldacchini, L. Valdevit, *Opt. Express* **2020**, 28, 20362.
- [47] C. Afting, P. Mainik, C. Vazquez-Martel, T. Abele, V. Kaul, G. Kale, K. Göpfrich, S. Lemke, E. Blasco, J. Wittbrodt, *Adv. Sci.* **2024**, 11, 2401110.
- [48] N. Munding, M. Fladung, Y. Chen, M. Hippler, A. D. Ho, M. Wegener, M. Bastmeyer, M. Tanaka, *Adv. Funct. Mater.* **2024**, 34, 2301133.
- [49] C. Zhou, S. J. Feng, S. Leong, E. Breil, F. Voruz, C. Valentini, D. R. Hammer, A. Aksit, E. S. Olson, J. Guo, J. W. Kysar, A. K. Lalwani, *Acad. Radiol.* **2025**, 32, 2152.
- [50] A. C. Davis, M. M. Howard, E. Z. Freeman, L. Solorio, D. J. Cappelleri, Mobile Microrobot Grippers for Cell Spheroid Micromanipulation, in *2024 Inter. Conf. on Manipulation, Automation and Robotics at Small Scales (MARSS)*, IEEE **2024**, pp. 1–6.